ANNALS OF GEOPHYSICS, 67, 4, S437, 2024; doi:10.4401/ag-9147
OPEN ACCESS

# A new view of seismicity under Mt. Etna volcano, Italy, 2014-2023 from multi-scale high-precision earthquake relocations

Anthony Lomax[*,1], Tiziana Tuvè[2], Elisabetta Giampiccolo[2], Ornella Cocina[2]

(1) ALomax Scientific, Mouans-Sartoux, France
(2) Istituto Nazionale di Geofisica e Vulcanologia, Osservatorio Etneo, Catania, Italy

Article history: received August 30, 2024; accepted September 18, 2024

## Abstract

Mt. Etna volcano in southern Italy, with a high rate of eruptive events and flank instability, poses a high hazard to surrounding, densely populated areas. Monitoring, hazard assessment and comprehension of Mt. Etna requires detailed knowledge of the structure and dynamics of the volcanic system across space-time scales. Here we relocate volcano-tectonic earthquakes from 2014 to 2023 at Mt. Etna with an enhanced location procedure which generates travel-time corrections to improve multi-scale precision and uses waveform similarity to improve fine-scale precision. Relative to previous studies, the relocated seismicity shows improved resolution of distinct patterns of organization and clustering at different space-time scales, and images novel features. Shallower than about 10 km depth, dense clusters dominate in the central part of the volcano, some concentrated within volumes of 0.5 km or less in extent, and mainly active for limited periods around the December 2018 and 2021-2022 eruptive episodes. These clusters likely indicate brittle fracturing due to stress changes from intrusive dykes adjacent to the clusters or from replenishment of a shallow, central magmatic reservoir preceding volcanic activity. Shallower seismicity surrounding the central clusters is composed of multi-scale, hierarchical clusters, bands and lineations of seismicity, some showing far-field response to intrusions over limited time periods and others active throughout the study periods and showing response to faulting and flank collapse in the volcanic edifice and to regional stress. Focal mechanism P- and T-axes for the shallower seismicity show clearly a previously identified radial symmetry, indicating pressurization strain sources concentrated under the summit area of the volcano. From about 10 to 25 km depth, diffuse and localized clusters of seismicity define an ~5 km or thinner, tabular surface plunging ~20° towards N30°W and characterized by NNW-SSE striking P-axes. This NNW plunging surface likely reflects thrusting below the volcanic cover due to NW oriented crustal convergence. Dense, elongated clusters of seismicity occur around 1-20 km depth, including two preceding an eruptive episode in 2021-2022 which may indicate magma movement and re-pressurization in the intermediate and deep crust.

Keywords: Etna Volcano; High-precision earthquake location; Seismicity; Volcano monitoring; Volcano dynamics

## 1. Introduction

Mt. Etna volcano is a strato-volcano located in eastern Sicily, southern Italy (Fig. 1). The volcanic edifice is characterized by a complex geodynamic setting resulting from the combination of regional tectonics and flank instability (Bousquet and Lanzafame, 2004; Bonforte et al., 2007). In particular, the eastern flank of the volcano is affected by a continuous ESE seaward sliding, a process that is ongoing due to the interrelationship between gravitational instability and magma intrusion.

In a volcano setting, seismic signals can arise from volcano-tectonic events due to brittle, shear or crack opening failure, or from long to very long period sources and tremor, due to processes involving magmatic or pore fluids and gasses, or mass movements (Chouet, 2003; Patanè et al., 2004; Cannata et al., 2013). Associating the space-time distribution of seismicity with volcano dynamics requires that seismic event locations are determined with high precision across multiple scales, where precision refers to the correctness of the relative position of located events. Numerous previous studies of Mt. Etna involve high-precision relocations using different methodologies (e.g., Brancato and Gresta, 2003; Alparone et al., 2020). In this study we obtain multi-scale high-precision relocations of volcano-tectonic seismicity from 2014 through 2023 at Mt. Etna using NLL-SSST-coherence (NLL-SC; Lomax and Savvaidis, 2022; Lomax and Henry, 2023). The NonLinLoc location algorithm (NLL; Lomax et al., 2000, 2014),

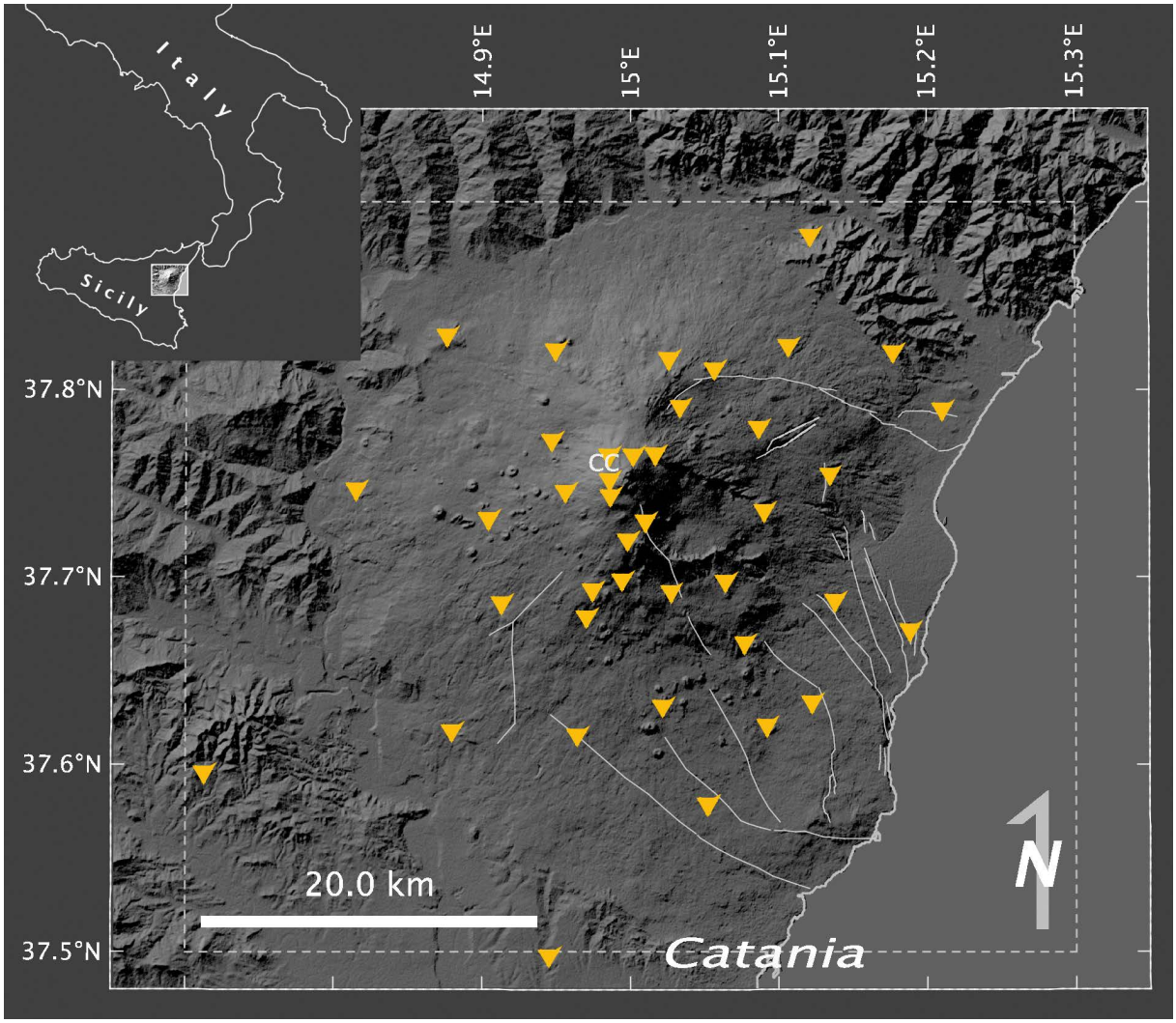


**Figure 1.** Map of the Mt. Etna volcano area showing seismic stations operating during 2014-2023 used for NLL-SC relocation (red triangles). Additional stations outside the map area were also used for relocation (see station coordinates in Supplementary File S1 and Movie S1). Dashed lines show the latitude-longitude limits for selection of INGV Osservatorio Etneo catalog events for relocation.

performs a global search to obtain a probabilistic solution for hypocenter locations and is applicable with 3D seismic velocity models. NLL-SC extends NLL with source-specific, station travel-time corrections (SSST) and inter-event waveform coherence to improve location precision across multiple spatial scales, typically ranging from the size of a study area down to around 100 m or less.

Application of NLL has improved understanding of the complex geophysical and volcanic processes and heterogeneity of the Earth's crust in dynamic volcanic environments such as in Italy. One of the earliest applications of NLL was relocation of seismicity from 1989 to 1998 under the Somma-Vesuvius volcano using a 3D velocity model (Lomax et al., 2001; Zollo et al., 2002). Relative to previous studies, the NLL relocated events fall within a shallower and much more concentrated volume, mainly in the upper 2 km of the Mesozoic carbonate basement underlying the Somma-Vesuvius complex. More recently, NL-SC has been applied to relocation of 2014-2023 seismicity under the Campi Flegrei caldera, which is experiencing sustained ground uplift and increasing seismicity since 2005 (Scotto di Uccio et al. 2024). These multi-scale precise NLL-SC relocations give improved identification and delineation of activated fault zones and help with structural reconstructions and hazard assessment for the caldera.

In the last decade, for the case of Mt. Etna, Mostaccio et al. (2013) and Alparone et al. (2013) used three-dimensional velocity models and the NLL probabilistic approach to improve the localization of seismicity in the eastern flank of the volcano. These authors analyzed the seismicity during 2002-2003, a period of significant eruptive activity (Mostaccio et al., 2013), and that associated with the Pernicana fault system, located on the north-eastern slope of Mount Mt. Etna. This fault is of interest due to its active tectonics and hazard; it links westward to the NE Rift and seems to have an important role in controlling instability processes affecting the eastern flank of the volcano (i.e., (Alparone et al., 2013).

Here we focus on NLL-SC relocation of volcano-tectonic seismicity at Etna volcano in the period 2014-2023, to provide a multi-scale high-precision catalog of the volcano and to improve understanding of eruptive processes and volcano dynamics. During the analyzed period several episodes of magma intrusion, eruptions and increase of seismicity are documented, including the December 2018 eruption and the violent paroxysmal events observed on the volcano from December 2020 to October 2021.

We examine larger scale and longer-term processes due to regional stress and deep magma recharge and storage, intermediate space-time scale processes including faulting, flank collapse and fluid migration, and smaller space-time scale dyke intrusions and eruptions. We also examine the distribution of P- and T-axes from composite, first-motion focal-mechanisms obtained for the relocated seismicity.

## 2. Multi-scale high-precision earthquake location

We obtain high-precision earthquake relocations across multi-scales with NLL-SSST-coherence (NLL-SC), which combines source-specific, station travel-time corrections (SSST) with weighted stacking of probabilistic locations for nearby event based on inter-event waveform coherence (Lomax and Savvaidis, 2022; Lomax and Henry, 2023). NLL-SC is based on the NonLinLoc location algorithm (Lomax et al., 2000, 2014); NLL hereafter), which performs efficient, global sampling to obtain an estimate of a posterior probability density function (PDF) in 3D space for hypocenter location. The PDF is a comprehensive description of likely hypocentral locations and related uncertainty for an event and enables application of the waveform coherence relocation. Within NLL, we use the equal differential-timing (EDT) likelihood function (Zhou, 1994; Font et al., 2004; Lomax, 2005; Lomax et al., 2014), which is highly robust in the presence of outlier data caused by large error in phase identification, measured arrival-times or predicted travel-times. We use a finite-differences, eikonal-equation algorithm (Podvin and Lecomte, 1991) to calculate gridded P and S travel-times for initial NLL locations.

### 2.1 Source-specific station travel-time corrections

In a first relocation stage, NLL-SC iteratively develops SSST corrections on collapsing length scales (Richards-Dinger and Shearer, 2000; Lomax and Savvaidis, 2022), which can greatly improve multi-scale, relative location correctness and clustering of events (Pavlis and Hokanson, 1985; Richards-Dinger and Shearer, 2000; Lin and Shearer, 2005;

Nooshiri et al., 2017). In contrast to station static corrections (Tucker et al., 1968; Ellsworth, 1975; Frohlich, 1979; Lomax, 2005, 2008), which give a unique time correction for each station and phase type, SSST corrections vary smoothly throughout a 3D volume to specify a source-position dependent correction for each station and phase type. These corrections account for 3D variations in velocity structure and corresponding distortion in source-receiver ray paths. NLL-SSST uses smooth, Gaussian distance kernels for accumulating SSST corrections, while Richards-Dinger and Shearer (2000) use a fixed number of neighboring events, and Lin and Shearer (2005) use fixed distance and shrinking-box approaches.

Spatial-varying, SSST corrections are most effective for improving relative locations across scales for which the ray paths between stations and events differ greatly across the studied seismicity, in particular when stations are inside the seismicity distribution, the extent of seismicity is large relative to the distance to the stations, or the depth range of events is large. SSST corrections can improve multi-scale precision when epistemic error in the velocity model is large, such as when a 1D, laterally homogeneous model or a smooth model is used in an area with lateral velocity contrasts or smaller scale, 3D heterogeneities. In general, SSST cannot compensate for location bias due to model error on the largest scales (e.g. the full study area).

## 2.2 Waveform coherence relocation

In a second relocation stage, NLL-SC reduces aleatoric location error by consolidating information across event locations based on waveform coherency between the events (Lomax and Savvaidis, 2022). This relocation, NLL-coherence, is based on the concept that if the waveforms at a station for two events are very similar (e.g. have high coherency) up to a given dominant frequency, then the distance separating these events is small relative to the seismic wavelength at that frequency (e.g., Geller and Mueller, 1980; Poupinet et al., 1984), perhaps less than about ¼ of this wavelength (Geller and Mueller, 1980; Thorbjarnardottir and Pechmann, 1987).

For detailed seismicity analysis, precise, differential times between like-phases (e.g. P and S) for pairs of nearby events can be measured through waveform correlation. Differential times from a sufficient number of stations allow high-precision, relative location between events, usually preserving the initial centroid of the event positions (Nakamura, 1978; Poupinet et al., 1982, 1984; Ito, 1985; Got et al., 1994; Nadeau et al., 1994; Waldhauser and Ellsworth, 2000; Brancato and Gresta, 2003; Matoza et al., 2013; Trugman and Shearer, 2017).

In contrast, NLL-coherence uses waveform similarity directly to improve relative location correctness without the need for differential time measurements or many stations with waveform data. The method assumes that high coherency between waveforms for two events implies the events are nearly co-located, and that all possible observed information that can constrain the event locations, when corrected for true origin-time shifts, should be nearly identical in the absence of noise. Then, stacking over probabilistic locations for nearby events can reduce the noise in this information and improve the location precision for individual, target events. We measure coherency as the maximum, absolute, normalized cross-correlation between waveforms from one or more stations for all pairs of events separated after NLL-SSST relocation by less than a specified distance (2.5 km in this study, which is roughly twice the extent of typical clustered seismicity in the final NLL-SSST relocations; see Supplementary Fig. S3). We take the maximum station coherence between the target event and each other event as a proxy for true inter-event distances and as weights to stack NLL-SSST location probability density functions (PDF's) over the events. In effect, this stack directly improves the hypocenter location for each target event by combining and completing arrival-time data over nearby events and reducing aleatoric measurement error in this data such as noise, outliers and missing arrivals.

For a ground-truth Test of NLL-SC using controlled-source, explosion data from Finland, Lomax and Savvaidis (2022) estimated a relative horizontal location error of about 75 m. See Lomax and Savvaidis (2022) and Lomax and Henry (2023) for more discussion, details and examples on NLL-SC, and Supplementary File S1 for NLL-SC processing parameters used in this study.

## 2.3 Coherence based, composite event focal mechanisms

First-motion focal mechanisms provide earthquake fault-plane orientations and slip directions, which, in turn, provide information on faulting geometry and the stress field around the earthquakes. Typically, first-motion

mechanisms are determined independently for each event from the distribution of P-wave arrival polarities on the focal sphere, under the constraint that the mechanism is pure double-couple. This determination can be done for the majority of events in a catalog, in particular for the numerous smaller events, but is often unstable or highly uncertain due an insufficient number of polarity readings, giving poor coverage of the focal sphere, or error in polarity of the readings (Hardebeck and Shearer, 2002).

The information on waveform similarity between nearby events can be used to greatly reduce the adverse effects on mechanism determinations due to lack of readings or polarity errors (Maurer and Deichmann, 1995; Shearer et al., 2003; Shelly et al., 2016). Here, using the waveform similarity measures determined by NLL-coherence, a composite set of polarity readings for each target event is formed with a maximum station coherence weighted stack over polarities from nearby events for each station. A target event may gain polarity readings for a given station even if a polarity for the station is not available for the target event. The stack forms a possibly enlarged and lower error, composite set of polarity readings for each event, while the resulting mechanisms are locally correlated across nearby events with similar waveforms.

Using these coherence-based composite readings, we determine first-motion double-couple focal mechanisms using FMAMP, which performs a probabilistic, global-search over focal mechanism strike, rake and dip using P-arrival, first-motion or amplitude data (Bernardi et al., 2015). FMAMP uses an efficient, oct-tree, importance sampling search (Lomax and Curtis 2001; Lomax et al. 2014), to determine ensembles of mechanisms that follow a probability density function for the mechanism as constrained by the data and evaluates solution quality based on weighted distribution of P and T axes. FMAMP is based in part on the HASH focal mechanism method (Hardebeck and Shearer, 2002). Ray take-off angles for each event are determined from the gradient at the event hypocenter of final, NLL-SSST travel-times for the corresponding stations and phase.

## 2.4 Seismic monitoring network

The seismic monitoring network on Mt. Etna in the analyzed period (Fig. 1) consisted of seismic stations equipped with broadband 3C velocimeter sensors, mainly Trillium 40s, gradually being replaced by Guralp CMG3EX 120s. The continuous process of technological renewal and upgrading of the Permanent Seismic Network (PSN) conducted by the INGV Osservatorio Etneo (INGV-OE) over the last twenty years has resulted in an increasingly high detection capacity, allowing a minimum local magnitude (ML) threshold of approximately 0.2 to be reached in some areas (Ferrari et al., 2024). Inter-station distances in the summit area are as low as 1-4 km, averaging about 1.5 km, allowing good location constraint for events with true hypocenter depth as shallow as roughly 1 km below the surface.

In the case of a seismic or volcanic crisis, including in areas geographically located outside the coverage of the PSN, the INGV-OE has a Mobile Seismic Network (MSN) which allows a temporary increase in the density of the permanent network and improves the detection and localization of earthquakes. The mobile network almost exclusively adopts Trillium Compact 120s sensors.

All permanent and temporary stations are in continuous, real-time acquisition and are sampled at a frequency of 100 Hz.

## 2.5 NLL-SSST-coherence relocation for Mt. Etna

For relocation under Mt. Etna in this study we use P and S arrival-times from the permanent network of the INGV-OE for about 15,200 volcano-tectonic events from 2014 through 2023 within the area latitude 37.5°N to 37.9°N, longitude 14.7°E to 15.3°E. We obtain initial NLL locations using a smooth, 1D velocity model (Etna1Dsmooth; Supplementary Fig. S1; model spreadsheet in Supplementary File S1) derived from the 1D velocity model used at INGV-OE for monitoring purposes (Hirn et al., 1991; Patanè et al., 1994). These initial locations do not use any static station time corrections, as equivalent corrections are determined in the first iteration of NLL-SSST corrections. We apply NLL-SSST with a smallest, Gaussian kernel smoothing length of 2 km and accumulate SSST travel-times on a cubic grid with 0.5 km spacing. We apply NLL-coherence using vertical component waveforms from 9 Mt. Etna seismic network stations band-pass filtered from 2-10 Hz frequency. The 10 Hz cutoff, under the ¼ of wavelength rule for typical separation of events with highly similar waveforms, implies a finest scale precision for the NLL-SC

relocations of about 100 m. Data and configuration files used to run the NLL-SSST-coherence relocations are provided in Supplementary File S1. Plots of the initial NLL locations, the final SSST relocations, and the NLL-SC relocations for all available events are shown in Supplementary Figs. S2-S4. A plot of the corresponding INGV-OE catalog locations is shown in Supplementary Figs. S5.

The resulting, formal NLL-SC epicenter (errH) and depth (errZ) uncertainties are as low as 100-200 m and generally less than 1 km (Fig. S6). This uncertainty range represents the correctness of relative location (precision) of the NLL-SC hypocenters plus the constraint on each location due to the geometry of stations with available picks, and the nominal and real error in the picks and final, SSST travel-times. This uncertainty does not include absolute, geographic location error – NLL-SC, like other location procedures, does not directly improve absolute, geographic epicenter and depth accuracy on the largest scales (e.g. the full study area), for which, in addition to a good station distribution and high-quality picks, an accurate initial velocity model and calibration with ground truth information is needed (Husen and Hardebeck, 2010). Thus, in the following, "multi-scale" precision ranges from approximately sub-km (as low as 100-200 m) to the extent of the study area, about 50 km.

We do not consider here two important issues that likely affect relocations for volcanic systems. One issue is temporal changes in the seismic wave velocities due to fluid and magma movement and other volcanic processes (Patanè et al., 2006; Cannata, 2012; Giampiccolo et al., 2020; De Gori et al., 2021). The other issue is reversal of waveform coherence and first-motion polarities for nearby events with otherwise similar waveforms, due to reversal slip on one of the two fault planes indicating local stress perturbations or fluid movement (Cesca et al., 2024 and references therein). Both of these issues can be accommodated in the NLL-SC procedure and future work should examine the occurrence, effect on relocations and mechanisms, and the implications of these effects.

The complete location solution produced by NLL and NLL-SC is a PDF in 3D space (latitude, longitude and depth) plus an implicit, optimal origin-time for each point in the PDF. Two hypocenters are determined: the maximum likelihood hypocenter at the maximum of the location PDF, and an expectation hypocenter at the center of a 68% confidence ellipsoid fit to the PDF (Lomax et al., 2000, 2014). In the following we analyze and plot expectation hypocenters since they avoid grid "pixelization" and overlap of maximum likelihood hypocenters from NLL-coherence which stacks event PDF's on a fine grid, and because they show the PDF centroids and thus can more stably recover the relative positions of NLL-coherence PDF's for nearby events. For better constrained locations the maximum-likelihood and expectation hypocenters are usually very similar.

## 3. Results

The NLL-SC relocated seismicity shows distinct patterns of clustering and alignment of seismicity over different space and time scales (Fig. 2; Supplementary Movies S1 and S2) and in different depth ranges (Fig. 3; all depths are below sea level – bsl). Epicenters are distributed throughout the ~40x40 km area covered by the volcanic edifice, with the highest concentrations of seismicity above about 10 km depth bsl (Fig. S6), towards the central part of the volcano, and below its eastern and southwestern flanks. Notably, there is little or no relocated seismicity within a high P-wave velocity body of breadth about 6-12 km from about 3-15 km depth bsl under the central-southeastern flank of the volcano, interpreted as solidified, high-density magma cumulates and clearly identified in tomography studies (e.g., Chiarabba et al., 2000; Patanè et al., 2006; Giampiccolo et al., 2020; De Gori et al., 2021).

The NLL-SC relocations are clearly more organized and clustered than the corresponding INGV-OE catalog locations (Supplementary Fig. S5) and show similar or increased organization and clustering compared to precise relocation in other recent studies of Mt. Etna, including those using double-difference relative location and joint inversion with 3D velocity models (e.g., Alparone et al. 2020; Mattia et al. 2020).

Much of the NLL-SC relocated seismicity (Fig. 2) is composed of isolated or nested hypocenter concentrations of different sizes and densities, forming diffuse bands of scales of 10 km or more, distinct clusters of up to around 10 km extent, and dense smaller clusters, streaks and filaments. The latter sometimes have one or more dimensions less than the nominal precision (~100-200 m) and formal uncertainties of the NLL-SC relocations (Fig. S6); the detailed geometry of the seismicity at such small scales is likely not robust with respect to the data set and processing parameters, but the presence of these concentrated features and their geometry on larger scales should be meaningful and valid for interpretation.

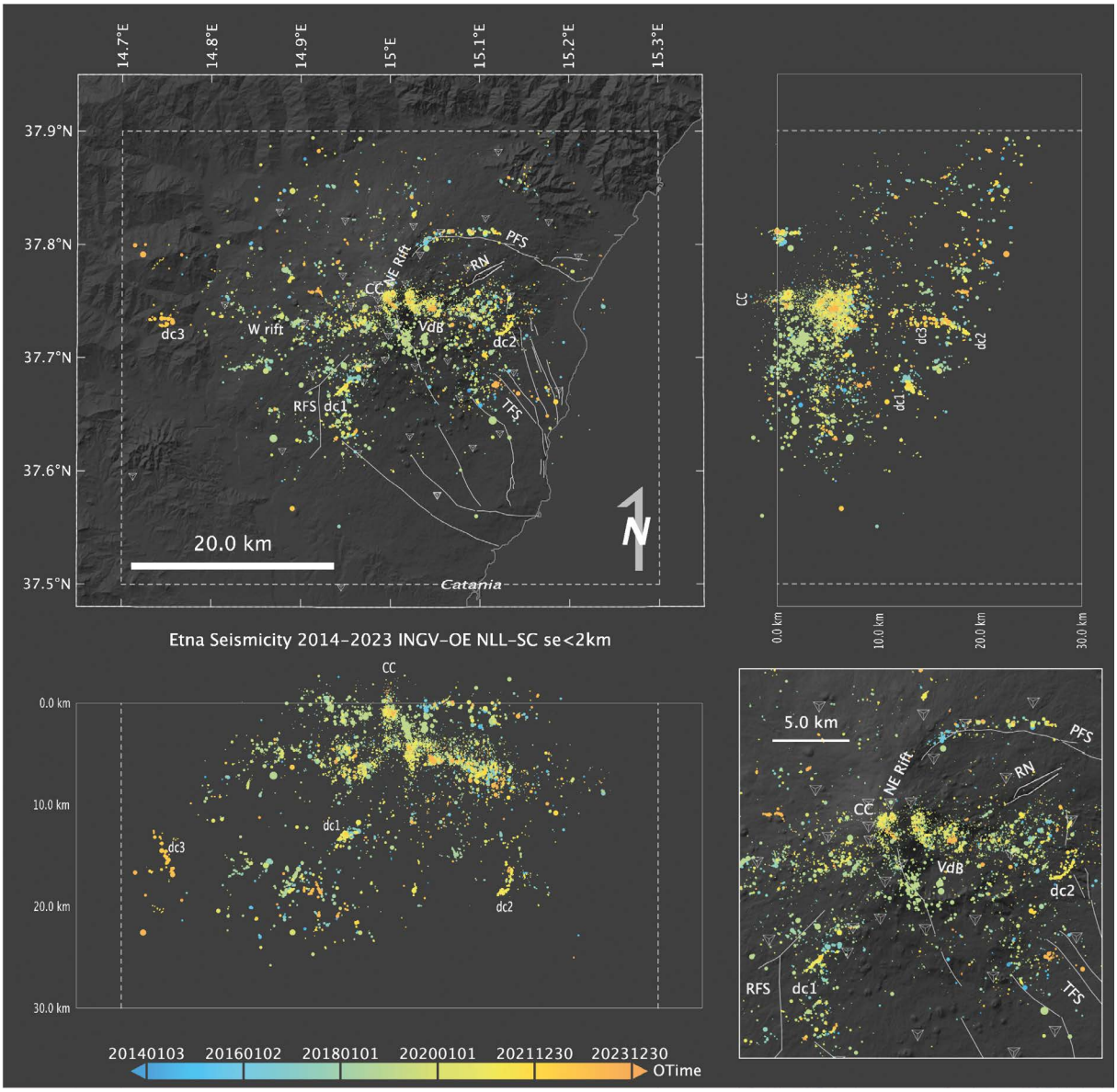


**Figure 2.** NLL-SC relocated seismicity 2014-2023. Expectation hypocenters for events with error ellipsoid semi-major axis (se) ≤ 2 km (11355 out of a total of 15199 relocated events) are shown with size proportional to magnitude and color indicating origin time. Gray triangles show seismic stations used for relocation. Light gray lines show surface traces of main faults (Azzaro et al., 2012). CC = Central Craters; VdB = Valle del Bove; PFS = Pernicana Fault System; RN = Ripe della Naca faults; TFS = Timpe Fault System; RFS = Ragalna Fault System; W rift = West Rift; dc1-3 = deep clusters 1-3. Dashed lines shows the latitude-longitude limits for selection of INGV-OE catalog events for relocation. The inset at the lower-right shows an expanded view of the map view seismicity in the central part of the volcanic edifice. Background topography from OpenTopography.org.

# 4. Discussion

## 4.1 Main features of the Mt. Etna seismicity

Above about 10 km depth the NLL-SC relocations show dense clusters which predominate in the central part of the volcano, and are surrounded, mainly to the east and southwest, by more diffuse, clustered and banded seismicity (Fig. 2; Supplementary Movies S1 and S2). The central clusters occur mainly from above sea-level to about 6 km depth, with two peaks of activity at around 1 km and about 3-5 km depth bsl (Fig. S6). Many are mainly active for limited periods, e.g. around the December 2018 and 2021-2022 eruptive episodes (Fig. S6; see Sec 3.2),

and are often concentrated and nested within volumes of 0.5 km or less in extent. The shallowest dense clusters, with a depth of about 1 km bsl, and an overlying column of sparse seismicity reaching ~2km km above sea-level are concentrated under the Central Craters area (CC in Fig. 3a).

The upper part of the sparse column of seismicity (see upper-left in Fig. 3a) locates between the Bocca Nuova crater (BN) and the Southeast Craters (SEC). Lava fountaining and other eruptive activity have occurred at the latter since 2021 (De Gori et al., 2021; Calvari et al., 2022), which suggests an absolute, geographic epicentral error of ≤ 0.5 km for the NLL-SC relocations in the summit area and other areas with dense station coverage (Fig. 1).

At less than 2 km bsl (Fig. 3a) the relocations show a narrow, ~8 km long, SW-NE to W-E curving alignment of earthquakes in the northeastern flank along the Pernicana Fault System (PFS). The PFS, with left-lateral and normal motion, has a significant role in shaping the deformation and decoupling the mobile, eastern flank of the volcano from the more stable part of the edifice (Acocella and Neri 2003; Solaro et al. 2010; Alparone et al. 2013; Ruch et al. 2013; Cannata et al. 2021). The NLL-SC relocations in the western 1/3 of this alignment (active mainly earlier in the study period) form a SW-NE trending plane dipping ~65° towards N150°E, and the eastern 2/3 (active mainly later in the study period) show a W-E trending vertical plane from just above sea-level to just below 2 km depth. The NLL-SC hypocenter of an M 4.2 earthquake on 2019-01-08, just after the December 2018 eruptive episode, locates at the base of the western plane. Other shallow clusters occur on the southeastern volcano flank at the western border of the Valle del Bove (VdB) (Fig. 3a).

From about 2-10 km depth bsl the seismicity surrounding the central part of the volcano forms a dense band or branch towards the east along the northern boundary of the VdB (Fig. 3b), including, to the northeast of the VdB, possible SW-NE trending splay-branches oriented sub-parallel to the Ripe della Naca faults just to the north.

Also at 2-10 km depth, there is diffuse seismicity within and to the south of the VdB, and further to the southeast and along the NW-SE trending, right-lateral trans-tensional, Timpe Fault System (see TFS in Fig. 2 and Fig. 3b). The latter hosts the largest event in the study period, the M 4.9 Fleri earthquake (Monaco et al., 2021; Tringali et al., 2023) on 2018-12-26 during the December 2018 eruptive episode, with NLL-SC depth ~1.5 km bsl. In the western sector, the seismicity depicts a W-E trending band of clusters along the West Rift, and dispersed clusters to the east and west of the Ragalna Fault System (see RFS in Fig. 3b).

The deeper NLL-SC relocated seismicity from about 10 to 25 km shows mainly sparse events and dense clusters (Fig. 3c), much of which defines an ~5 km or thinner, tabular surface dipping ~20° towards N30°W (Fig. 4;

(a)

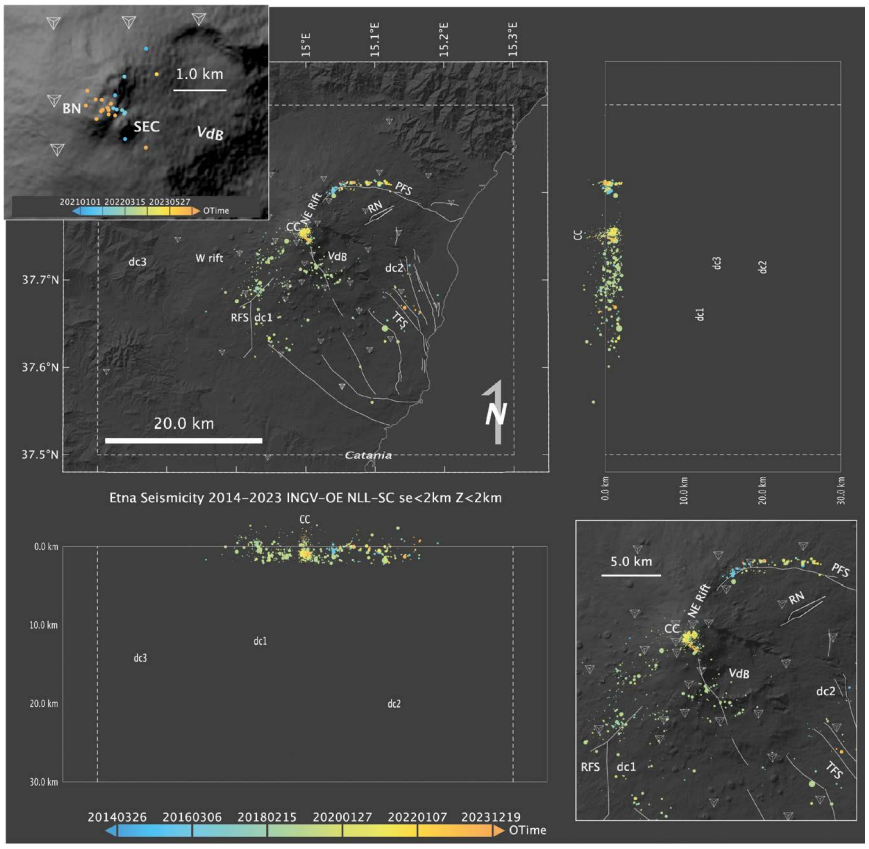

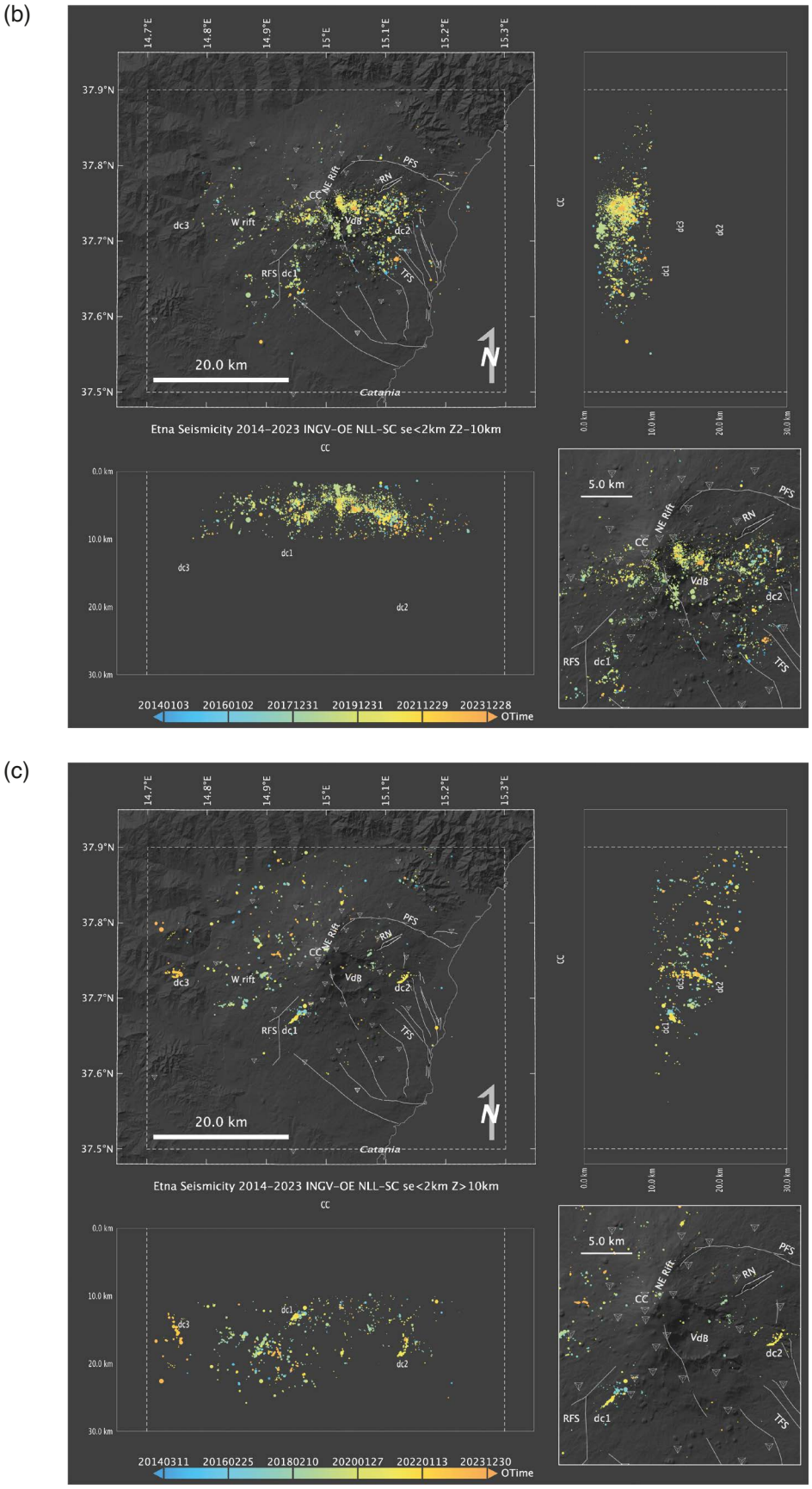


**Figure 3.** Depth intervals of NLL-SC relocated seismicity 2014-2023. (a) above 2 km depth bsl; (b) 2-10 km bsl; (c) below 10 km bsl. Expectation hypocenters for all locations with error ellipsoid semi-major axis (se) $\leq 2$ km are shown, with other map elements as in Fig. 2. The upper-left inset in panel (a) shows relocated seismicity shallower than 1 km above sea-level during 2021-2023 in the Central Craters area; BN = Bocca Nuova; SEC = South East crater.

Supplementary Movie S2). This surface is likely related to crustal convergence towards the NW that takes place beneath the volcanic cover, and may be identified as a SE verging thrust ramp, perhaps the Sicilian Basal Thrust Lavecchia et al., 2007; De Guidi et al., 2015; Barreca et al., 2020; Firetto Carlino et al., 2022; Scarfì et al., 2023; Lo Bue et al., 2024).

Two distinct clusters of seismicity (dc1 and dc2 in Figs. 3c and 4). are identified both to the southwest and to the east in the depth range 12-20 km; these clusters have been interpreted as first indicators of new magma ascent

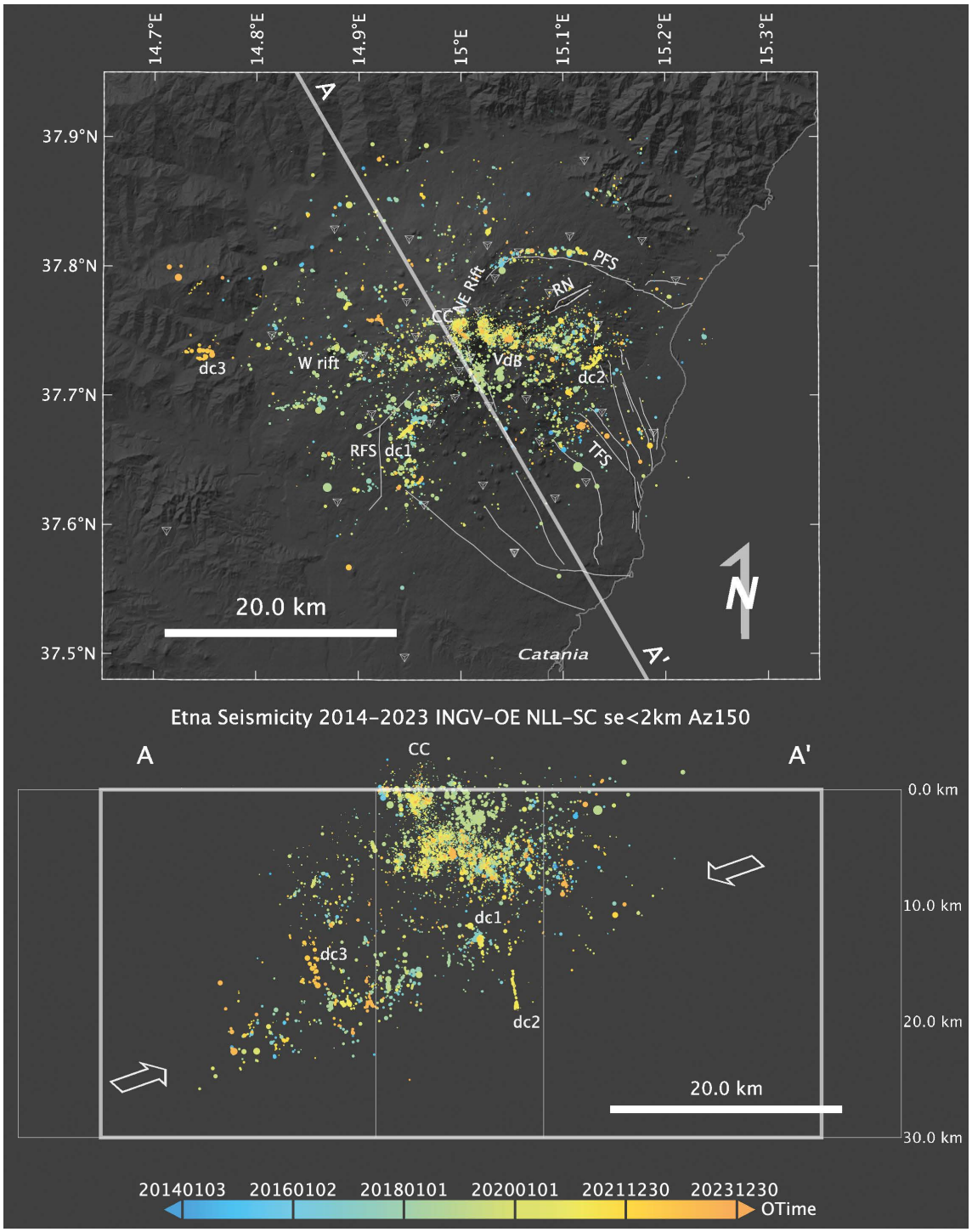


**Figure 4.** N30°W-N150°E profile view of NLL-SC relocated seismicity 2014-2023 showing how most seismicity below around 10 km depth bsl falls near a surface dipping ~20° towards N30°W (indicated by large arrows). dc1-3 = deep clusters 1-3. Expectation hypocenters for all locations with error ellipsoid semi-major axis (se) ≤ 2 km are shown, with other map elements as in Fig. 2.

from a mantle source (e.g., De Gori et al., 2021). The NLL-SC relocations image these and some other deeper clusters as narrow, elongated, and sometimes filament-like, suggesting a brittle response to concentrated stress along or beyond (Rubin and Gillard, 1998) the edges of a primary or branching magma pathway. Another distinct, isolated cluster beyond the western limit of the volcano edifice at around 15 km depth (dc3 in Figs. 3c and 4), active mainly from August 2022 to February 2023, is probably related to crustal or regional stresses and not directly to volcanic activity.

## 4.2 Focal mechanism P and T axes and stress

From the NLL-SC relocation results, we generate composite, coherence-based focal mechanisms (Sec. 2.3) for events with at least 20 composite reading. The P-axes for these mechanisms (Fig. 5a) have strikes consistent with that of many of the main structures and a more or less radial geometry, while the T-axes (Fig. 5b) generally form concentric rings. These results broadly align with the findings of previous studies and indicate radial compression from one or more pressurization strain sources under and close to the summit area of the volcano (e.g., Patanè and Privitera, 2001; Patanè et al., 2003; Musumeci et al., 2004; Alparone et al., 2020; Scarfì et al., 2023). Moreover, the radial pattern of P-axes is also echoed in a recent P-wave anisotropic tomography study which shows a clear radial trend of the fast axis (Lo Bue et al., 2024).

One exception to the overall radial distribution of P-axes is a nearly constant, NNW-SSE strike of P-axes for deeper events under the NW flank of the volcano (Fig. 5a). As these events lie on the tabular surface plunging towards N30°W (Fig. 4), these P-axes orientations suggest the stress across this surface is mainly regional and not primarily due to central strain sources under the volcano.

Also, at shallow depths $< 5$ km bsl the P- and T-axes orientations are often coherent with the strike of the main faults. For example, SW-NE P-axes and NW-SE T-axes reflect left-lateral motion along the PFS (Fig. 5).

## 4.3 Mt. Etna seismicity during two eruptive episodes

Much of the seismicity under Mt. Etna occurs within limited periods. Seismicity during eruptive episodes in December 2018 and 2021-2022 accounts for almost half of all relocated seismicity in the period 2014-2023.

The 2018 Mt. Etna flank eruption (Bonforte et al., 2019; Alparone et al., 2020; Giampiccolo et al., 2020; Mattia et al., 2020) was preceded by increased seismicity throughout the volcano edifice starting in October 2017. Anomalous ground deformation, volcanic tremor and intense volcano-tectonic seismicity in the summit area of the volcano began on in the morning of December 24, 2018, followed by opening of an eruptive fissure that propagated towards the SE from the central craters and remained active through December 27 (Fig. 6a). The majority of the seismicity in this period occurred during the first 24 hours. Following Alparone et al. (2020; their Fig. 4c), we consider the NLL-SC relocations for December 24-25, 2018, plotted in Fig. 6a. These relocations show the main evolution of the seismicity as identified by Alparone et al. (2020). The earliest events (December 24, 08:30-10:30 UTC) cluster at shallow depths under the summit craters at the northern end of the eruptive fissure, with scattered events to the east, and to the west within and at the western head of the VdB. In the next hours (10:30-16:30 UTC), seismicity initiates around the southern end of the eruptive fissure along the southwestern wall of the VdB. Later seismicity (from 16:30 UTC) migrates deeper, to the south and east along the southern wall of the VdB, and towards the west.

In general, the NLL-SC hypocenters are about 1 km deeper, less dispersed and form tighter (often nested) clusters relative to those shown by Alparone et al. (2020). The disposition of NLL-SC epicenters along the curving, southwestern and south walls of the VdB (Fig. 6a), along with a prevalence in this area of normal faulting mechanisms and roughly SW-NE T-axes oriented near-perpendicular to the walls (Fig 5b), suggest this seismicity reflects extensional sliding of the VdB towards the NE, likely a component of the larger scale deformation and eastward motion of the unstable eastern flank during the 2018 unrest episode (Bonforte et al., 2019; Alparone et al., 2020; Giampiccolo et al., 2020; Mattia et al., 2020). The size, distribution and orientation in both epicenter and depth of NLL-SC seismicity clusters in Fig. 6a is remarkably similar to that determined for the July-August 2001 lateral eruption at Mt. Etna (Musumeci et al., 2004; their Fig. 1), indicating similar stress sources and dyke geometry at depth, as well as ensuing volcano and flank dynamics, for the 2001 and 2018 eruptive episodes, as proposed previously (e.g., Bonforte et al., 2019; Mattia et al., 2020).

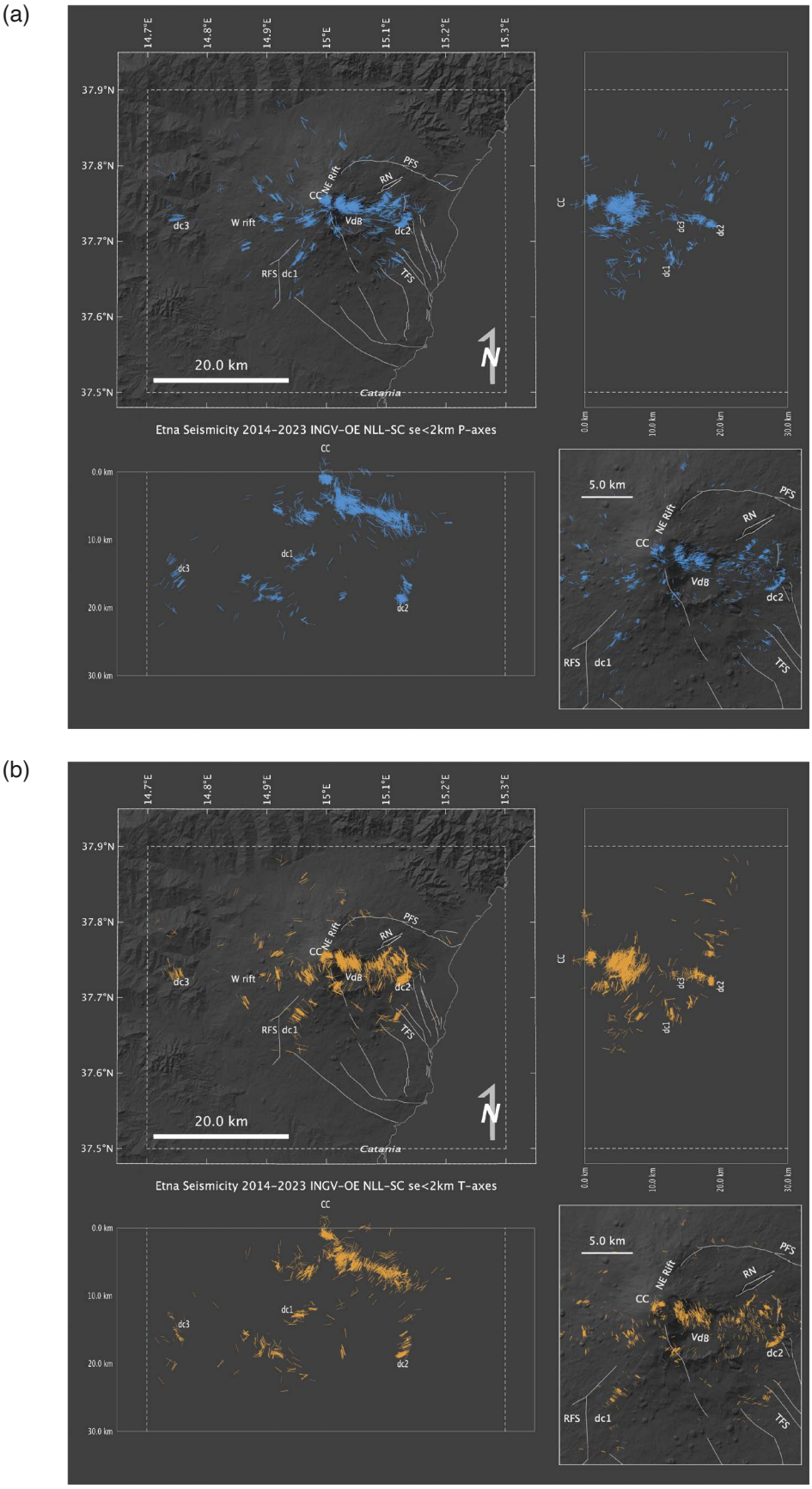


**Figure 5.** P and T axes for FMAMP composite, first-motion focal-mechanism for NLL-SC relocated seismicity 2014-2023. (a) P (compressional) and (b) T (extensional) axes for focal-mechanisms with 20 or more, composite P-wave polarity readings and FMAMP misfit $\leq 0.15$, where misfit is the proportion of weighted polarity errors in the optimal solution. Other map elements as in Fig. 2.

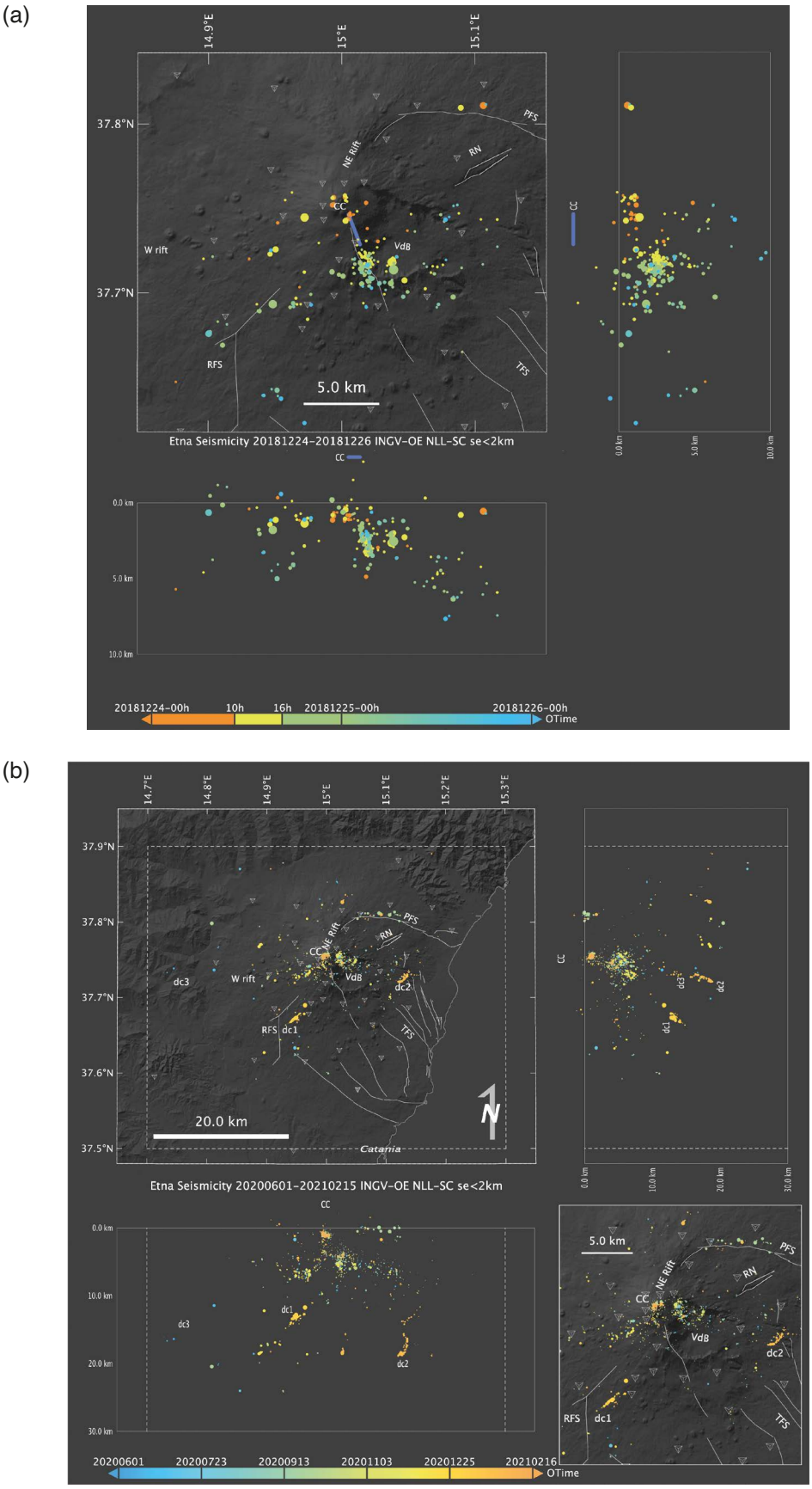


**Figure 6.** NLL-SC relocated seismicity during eruptive episodes. (a) 2017-10-01 through 2019-02-28 in the central part of the volcano; blue bar shows approximate position of December 24-27 2018 eruptive fissure. (b) 2020-06-01 through 2021-02-15. Expectation hypocenters for all locations with error ellipsoid semi-major axis (se) ≤ 2 kmare shown, with other map elements as in Fig. 2.

After almost 1 year of stability, a gradual increase in VT seismicity was observed from late June 2020 mainly involving the shallower part of the central area of the volcano. Starting in December 2020, volcanic activity increased with some paroxysmal events, and geochemical, petrological, ground deformation and seismological data indicated a significant event of magma transfer from the deepest sources to the surface (see INGV-OE weekly reports). In this period the VT seismicity increase was characterized also by high strain releases and occurrence rate mainly related to the occurrence of seismic swarms in the summit area and along the south western and eastern flanks in the intermediate and deep levels (De Gori et al., 2021). On February 16, 2021 an intense phase of 57 lava fountain episodes at the Southeast crater started (Andronico et al., 2024), accompanied by a drastic reduction in the shallower seismicity.

The NLL-SC seismicity during the 8.5 month preceding this activity (Fig. 6b) shows the main clusters which characterized this period, leading to the parossistic phase:

- the shallowest events which occurred under the summit craters at around 1 km depth bsl (near CC in Fig. 6b), within a volume of about 1 km in extent, formed of nested, sub-clusters of less than 0.5 km in extent.
- the two deeper clusters of seismicity in the southwestern and eastern flank which characterized the sharp increase of seismicity from December 2020 through January 2021. The southwestern cluster (dc1 in Fig. 6b) is essentially a swarm which occurred on December 31, 2020 at intermediate depths between 10 and 15 km bsl with a SW-NE spread of epicenters. The cluster in the eastern flank (dc2 in Fig 6b) is a seismic swarm which occurred on January 24, 2021 at focal depths mainly between 15 and 19 km bsl plus scattered shallower events around 13 km bsl, and which also shows SW-NE oriented epicenters.

The shallowest clusters in both of these eruptive episodes likely indicate brittle fracturing due to stress changes from nearby intrusive dykes (Brancato and Gresta, 2003; Alparone et al., 2020) or replenishment of the shallow central magmatic reservoir preceding volcanic activity (Bonaccorso et al., 2021; De Gori et al., 2021). Seismic swarms located in the intermediate and deep volumes in the western, south western and eastern flanks usually occurred before Etna eruptive phases and are interpreted as a response to the stress induced by the magma movement toward the surface and by reservoir re-pressurization (Alparone et al., 2012; Sicali et al., 2015; Bonaccorso et al., 2021; De Gori et al., 2021).

## 5. Conclusions

Multi-scale high-precision relocation of volcano-tectonic seismic events at Mt. Etna from 2014 through 2023 using NLL-SSST and NLL-coherence shows improvements in organization and clustering of seismicity over previous studies, including those using double-difference relative location and joint inversion with 3D velocity models. The relocated seismicity (Fig. 2; Supplementary Movies S1 and S2) includes hypocenter concentrations of different sizes and densities, including diffuse bands of scales of 10 km or more, nested clusters of up to around 10 km extent, and dense smaller clusters, streaks and filaments. The NLL-SC relocations show well established features of the Mt. Etna seismicity including occurrence of most events at shallower than about 10 depth bsl, within the central part of the volcano and below its eastern and southwestern flanks, little or no relocated seismicity within a high P-wave velocity body under the central-southeastern flank of the volcano, and P- and T-axes for composite, NLL-SC focal mechanisms recover a radial symmetry due to pressurization strain sources localized under the summit area of the volcano (Fig. 5).

A number of notable and novel features of Mt. Etna seismicity are well resolved in the NLL-SC relocations. These include dense, nested clusters above about 6 km depth around and under the Central Craters area, some within volumes of as little as 0.5 km or less in extent. Along the Pernicana Fault System (PFS) the relocations show (Fig. 3a) a narrow, SW-NE to W-E curving alignment of earthquakes at less than 2 km depth bsl, possibly consisting of two planar surfaces with different dips, and focal mechanism P-axes and T-axes consistent with left-lateral motion along the PFS (Fig. 5).

At greater depths, the relocations image a <5 km thick, tabular surface from about 10 to 25 km depth with dip ~20° towards N30°W, possibly a thrust ramp related to NW crustal convergence (Fig. 4). At around 12 to 20 km depth, the NLL-SC relocations resolve dense, isolated clusters of seismicity, two of which (dc1 and dc2 in, e.g., Figs. 2, 3c, 4 and 6b) may be caused by magma ascent and recharge. NLL-SC images these deeper clusters as elongated and narrow, suggesting that the seismicity is aligned near-vertically along magma pathways.

The NLL-SC hypocenters for two days of intense activity during the 2018 Mt. Etna flank eruption (Fig. 6a) show concentrated and often nested clusters under the central craters and eruptive fissure, likely a response to intrusive dikes feeding the eruption, and along the curving, southwestern and south walls of the VdB, reflecting extensional sliding of the upper VdB towards the NE. The distribution of NLL-SC seismicity is remarkably similar to that found for the July-August 2001 lateral eruption at Mt. Etna (Musumeci et al., 2004), suggesting similar stress and magma sources, and volcano dynamics for the two eruptive episodes.

NLL-SC relocations for 8.5 months preceding intense lava fountaining in 2021 at the Central Craters (Fig. 6b) show an increasing seismicity rate mainly involving shallow, concentrated, nested clusters under the crater area, as well as deeper clusters at > 10 km depth bsl (dc1-2 in Fig. 6b). Seismicity just before the lava fountaining occurs mainly in the shallow and deeper clusters, likely reflecting magma movement and re-pressurization changes at both depths.

Multi-scale precise relocations and focal mechanisms of volcano-tectonic seismic events at Mt. Etna show in detail the effects at depth of the activity and dynamics of the volcano, while also underlining the variety, complexity and interactions of physical processes involved. The volcano-tectonic seismicity illuminates rapid strain-release events within the volcanic edifice, reflecting not just slip on principal faults, but more generally the response of fractured, brittle rock volumes, where present, to strain changes from nearby or distant magma movement and fracture processes, to larger scale motion and collapse of the volcanic edifice, and to regional tectonic deformation. Comprehensive interpretation of volcano-tectonic seismicity and understanding of the activity, dynamics and hazard of a structure like Mt. Etna requires interpretation within a general context of a space-time limited, brittle response to diverse strain sources across scales, and integration with constraints and results from all available geologic, geochemical, geophysical and geodetic observations.

**Data availability statement.** The relocated NLL-SC catalog, pick data, configuration and other files used to run the NLL-SC relocations presented in this study are provided in Supplementary File S1 and the catalog in a CSV file, both available at https://doi.org/10.5281/zenodo.13862396; the Mt. Etna seismic network stations have network code IV and station codes from EBCN to EVRN. INGV-OE weekly reports are available at: https://www.ct.ingv.it/index.php/monitoraggio-e-sorveglianza/prodotti-del-monitoraggio/bollettini-settimanali-multidisciplinari.

**Acknowledgements.** We wish to thank the INGV-OE seismic technical staff who ensured the regular working of the seismic monitoring network and the Gruppo Analisi Dati Sismici for providing manual picking and 1D earthquake locations. This study has benefited from funding provided by the Italian Presidenza del Consiglio dei Ministri – Dipartimento della Protezione Civile (DPC). This paper does not necessarily represent DPC official opinion and policies.

## References

Acocella, V. and M. Neri (2003). What makes flank eruptions? The 2001 Etna eruption and its possible triggering mechanisms, Bull. Volcanol., 65, 517-529, doi:10.1007/s00445-003-0280-3.

Alparone, S., G. Barberi, O. Cocina, E. Giampiccolo et al. (2012). Intrusive mechanism of the 2008-2009 Mt. Etna eruption: Constraints by tomographic images and stress tensor analysis, J. Volcanol. Geotherm. Res., 229-230, 50-63, doi:10.1016/j.jvolgeores.2012.04.001.

Alparone, S., G. Barberi, E. Giampiccolo, V. Maiolino et al. (2020). Seismological constraints on the 2018 Mt. Etna (Italy) flank eruption and implications for the flank dynamics of the volcano, Terra Nova, 32, 334-344, doi:10.1111/ter.12463.

Alparone, S., O. Cocina, S. Gambino, A. Mostaccio et al. (2013). Seismological features of the Pernicana-Provenzana Fault System (Mt. Etna, Italy) and implications for the dynamics of northeastern flank of the volcano, J. Volcanol. Geotherm. Res., 251, 16-26, doi:10.1016/j.jvolgeores.2012.03.010.

Andronico, D., C. D'Oriano, F. Pardini, A. La Spina et al. (2024). The 23-24 March 2021 lava fountain at Mt Etna, Italy, Bull. Volcanol., 86, 56, doi:10.1007/s00445-024-01745-5.

Azzaro, R., S. Branca, K. Gwinner and M. Coltelli (2012). The volcano-tectonic map of Etna volcano, 1:100.000 scale: an integrated approach based on a morphotectonic analysis from high-resolution DEM constrained by geologic, active faulting and seismotectonic data, Ital. J. Geosci., 131, 153-170, doi:10.3301/IJG.2011.29.

Barreca, G., S. Branca, R. A. Corsaro, L. Scarfì et al. (2020). Slab Detachment, Mantle Flow, and Crustal Collision in Eastern Sicily (Southern Italy): Implications on Mount Etna Volcanism. Tectonics, 39, e2020TC006188, doi:10.1029/2020TC006188.

Bernardi, F., A. Lomax, A. Michelini, V. Lauciani et al. (2015). Appraising the Early-est earthquake monitoring system for tsunami alerting at the Italian Candidate Tsunami Service Provider, Nat. Hazards Earth Syst. Sci., 15, 2019-2036, doi:10.5194/nhess-15-2019-2015.

Bonaccorso, A., L. Carleo, G. Currenti and A. Sicali (2021). Magma Migration at Shallower Levels and Lava Fountains Sequence as Revealed by Borehole Dilatometers on Etna Volcano, Front. Earth Sci., 9, Frontiers, doi:10.3389/feart.2021.740505.

Bonforte, A., S. Branca and M. Palano (2007). Geometric and kinematic variations along the active Pernicana fault: Implication for the dynamics of Mount Etna NE flank (Italy). J. Volcanol. Geotherm. Res., 160, 210-222, doi:10.1016/j.jvolgeores.2006.08.009.

Bonforte, A., F. Guglielmino and G. Puglisi (2019). Large dyke intrusion and small eruption: The December 24, 2018 Mt. Etna eruption imaged by Sentinel-1 data, Terra Nova, 31, 405-412, doi:10.1111/ter.12403.

Bousquet, J. C. and G. Lanzafame (2004). The Tectonics and Geodynamics of Mt. Etna: Synthesis and Interpretation of Geological and Geophysical Data, in Mt. Etna: Volcano Laboratory, 29-47, American Geophysical Union (AGU), doi:10.1029/143GM03.

Brancato, A. and S. Gresta (2003). High precision relocation of microearthquakes at Mt. Etna (1991-1993 eruption onset): a tool for better understanding the volcano seismicity, J. Volcanol. Geotherm. Res., 124, 219-239, doi:10.1016/S0377-0273(03)00071-4.

Calvari, S., E. Biale, A. Bonaccorso, A. Cannata et al. (2022). Explosive Paroxysmal Events at Etna Volcano of Different Magnitude and Intensity Explored through a Multidisciplinary Monitoring System, Remote Sens., 14, 4006, Multidisciplinary Digital Publishing Institute, doi:10.3390/rs14164006.

Cannata, A. (2012). Crustal changes at Mt. Etna volcano accompanying the 2002-2003 eruption as inferred from a repeating earthquake analysis, Geophys. Res. Lett., 39, doi:10.1029/2012GL053185.

Cannata, A., G. Di Grazia, M. Aliotta, C. Cassisi et al. (2013). Monitoring Seismo-volcanic and Infrasonic Signals at Volcanoes: Mt. Etna Case Study. Pure Appl. Geophys., 170, 1751-1771, doi:10.1007/s00024-012-0634-x.

Cannata, A., A. Iozzia, S. Alparone, A. Bonforte et al. (2021). Repeating earthquakes and ground deformation reveal the structure and triggering mechanisms of the Pernicana fault, Mt. Etna, Commun. Earth Environ., 2, 1-11, Nature Publishing Group, doi:10.1038/s43247-021-00188-6.

Cesca, S., P. Niemz, T. Dahm and S. Ide (2024). Anti-repeating earthquakes and how to explain them, Commun. Earth Environ., 5, 1-11, Nature Publishing Group, doi:10.1038/s43247-024-01290-1.

Chiarabba, C., A. Amato, E. Boschi and F. Barberi (2000). Recent seismicity and tomographic modeling of the Mount Etna plumbing system, J. Geophys. Res., Solid Earth, 105, 10923-10938, doi:10.1029/1999JB900427.

Chouet, B. (2003). Volcano Seismology, Pure Appl. Geophys., 160, 739-788, doi:10.1007/PL00012556.

De Gori, P., E. Giampiccolo, O. Cocina, S. Branca et al. (2021). Re-pressurized magma at Mt. Etna, Italy, may feed eruptions for years, Commun. Earth Environ., 2, 1-9, Nature Publishing Group, doi:10.1038/s43247-021-00282-9.

De Guidi, G., G. Barberi, G. Barreca, V. Bruno et al. (2015). Geological, seismological and geodetic evidence of active thrusting and folding south of Mt. Etna (eastern Sicily): Revaluation of "seismic efficiency" of the Sicilian Basal Thrust, J. Geodyn., 90, 32-41, doi:10.1016/j.jog.2015.06.001.

Ellsworth, W. L. (1975). Bear Valley, California, earthquake sequence of February-March 1972, B. Seismol. Soc. Am., 65, 483-506, doi:10.1785/BSSA0650020483.

Ferrari, F., E. Giampiccolo, C. Musumeci, G. Tusa et al. (2024). La sismicità dell'area etnea nel periodo Gennaio – Dicembre 2021, 32, 4.4 MB, Istituto Nazionale di Geofisica e Vulcanologia (INGV), doi:10.13127/QDG/192.

Firetto Carlino, M., L. Scarfì, F. Cannavò, G. Barberi et al. (2022). Frequency-magnitude distribution of earthquakes at Etna volcano unravels critical stress changes along magma pathways, Commun. Earth Environ., 3, 1-13, Nature Publishing Group, doi:10.1038/s43247-022-00398-6.

Font, Y., H. Kao, S. Lallemand, C. S. Liu et al. (2004). Hypocentre determination offshore of eastern Taiwan using the Maximum Intersection method, Geophys. J. Int., 158, 655-675, doi:10.1111/j.1365-246X.2004.02317.x.

Frohlich, C. (1979). An efficient method for joint hypocenter determination for large groups of earthquakes, Comput. Geosci., 5, 387-389, doi:10.1016/0098-3004(79)90034-7.

Geller, R. J. and C. S. Mueller (1980). Four similar earthquakes in central California, Geophys. Res. Lett., 7, 821-824, doi:10.1029/GL007i010p00821.

Giampiccolo, E., O. Cocina, P. De Gori and C. Chiarabba (2020). Dyke intrusion and stress-induced collapse of volcano flanks: The example of the 2018 event at Mt. Etna (Sicily, Italy), Sci. Rep., 10, 6373, Nature Publishing Group, doi:10.1038/s41598-020-63371-3.

Got, J. L., J. Fréchet and F. W. Klein (1994). Deep fault plane geometry inferred from multiplet relative relocation beneath the south flank of Kilauea, J. Geophys. Res., 99, 15375, doi:10.1029/94JB00577.

Hardebeck, J. L. and P. M. Shearer (2002). A New Method for Determining First-Motion Focal Mechanisms, B. Seismol. Soc. Am., 92, 2264-2276, GeoScienceWorld, doi:10.1785/0120010200.

Hirn, A., A. Nercessian, M. Sapin, F. Ferrucci et al. (1991). Seismic heterogeneity of Mt Etna: structure and activity, Geophys. J. Int., 105, 139-153, doi:10.1111/j.1365-246X.1991.tb03450.x.

Husen, S. and J. Hardebeck (2010). Earthquake location accuracy, Community Online Resource for Statistical Seismicity Analysis, doi:10.5078/CORSSA-55815573.

Ito, A. (1985). High Resolution Relative Hypocenters of Similar Earthquakes by Cross-Spectral Analysis Method, J. Phys. Earth, 33, 279-294, doi:10.4294/jpe1952.33.279.

Lavecchia, G., F. Ferrarini, R. de Nardis, F. Visini et al. (2007). Active thrusting as a possible seismogenic source in Sicily (Southern Italy): Some insights from integrated structural-kinematic and seismological data, Tectonophysics, 445, 145-167, doi:10.1016/j.tecto.2007.07.007.

Lin, G. and P. Shearer (2005). Tests of relative earthquake location techniques using synthetic data, J. Geophys. Res., Solid Earth, 110, doi:10.1029/2004JB003380.

Lo Bue, R., F. Rappisi, M. Firetto Carlino, E. Giampiccolo et al. (2024). Crustal Structure of Etna Volcano (Italy) From P-Wave Anisotropic Tomography, Geophys. Res. Lett., 51, e2024GL108733, doi:10.1029/2024GL108733.

Lomax, A. (2005). A Reanalysis of the Hypocentral Location and Related Observations for the Great 1906 California Earthquake, B. Seismol. Soc. Am., 95, 861-877, doi:10.1785/0120040141.

Lomax, A. (2008). Location of the Focus and Tectonics of the Focal Region of the California Earthquake of 18 April 1906, B. Seismol. Soc. Am., 98, 846-860, doi:10.1785/0120060405.

Lomax, A. and A. Curtis (2001). Fast, probabilistic earthquake location in 3D models using oct-tree importance sampling, Geophys. Res. Abstr., Vol. 3, p. 955.

Lomax, A. and P. Henry (2023). Major California faults are smooth across multiple scales at seismogenic depth, Seismica, 2, doi:10.26443/seismica.v2i1.324.

Lomax, A., A. Michelini and A. Curtis (2014). Earthquake Location, Direct, Global-Search Methods, in Encyclopedia of Complexity and Systems Science, 1-33, R. A. Meyers (Editor), Springer, New York, doi:10.1007/978-3-642-27737-5_150-2.

Lomax, A. and A. Savvaidis (2022). High-Precision Earthquake Location Using Source-Specific Station Terms and Inter-Event Waveform Similarity, J. Geophys. Res., Solid Earth, 127, e2021JB023190, doi:10.1029/2021JB023190.

Lomax, A., J. Virieux, P. Volant and C. Berge-Thierry (2000). Probabilistic Earthquake Location in 3D and Layered Models, in Advances in Seismic Event Location, Modern Approaches in Geophysics, 18, 101-134, C. H. Thurber and N. Rabinowitz (eds.), Springer, Netherlands, doi:10.1007/978-94-015-9536-0_5.

Lomax, A., A. Zollo, P. Capuano and J. Virieux (2001). Precise, absolute earthquake location under Somma-Vesuvius volcano using a new three-dimensional velocity model, Geophys. J. Int., 146, 313-331, doi:10.1046/j.0956-540x.2001.01444.x.

Matoza, R. S., P. M. Shearer, G. Lin, C. J. Wolfe et al. (2013). Systematic relocation of seismicity on Hawaii Island from 1992 to 2009 using waveform cross correlation and cluster analysis, J. Geophys. Res., Solid Earth, 118, 2275-2288, doi:10.1002/jgrb.50189.

Mattia, M., V. Bruno, E. Montgomery-Brown, D. Patanè et al. (2020). Combined Seismic and Geodetic Analysis Before, During and After the 2018 Mount Etna Eruption, Geochem. Geophy. Geosy., 21, e2020GC009218, doi:10.1029/2020GC009218.

Maurer, H. and N. Deichmann (1995). Microearthquake cluster detection based on waveform similarities, with an application to the western Swiss Alps, Geophys. J. Int., 123, 588-600, doi:10.1111/j.1365-246X.1995.tb06873.x.

Monaco, C., G. Barreca, D. Bella, F. Brighenti et al. (2021). The seismogenic source of the 2018 December 26$^{th}$ earthquake (Mt. Etna, Italy): A shear zone in the unstable eastern flank of the volcano, J. Geodyn., 143, 101807, doi:10.1016/j.jog.2020.101807.

Mostaccio, A., T. Tuvè, D. Patanè, G. Barberi et al. (2013). Improving Seismic Surveillance at Mt. Etna Volcano by Probabilistic Earthquake Location in a 3D Model, B. Seismol. Soc. Am., 103, 2447-2459, doi:10.1785/0120110202.

Musumeci, C., O. Cocina, P. De Gori and D. Patanè (2004). Seismological evidence of stress induced by dike injection during the 2001 Mt. Etna eruption, Geophys. Res. Lett., 31, doi:10.1029/2003GL019367.

Nadeau, R., M. Antolik, P. A. Johnson, W. Foxall et al. (1994). Seismological studies at Parkfield III: Microearthquake clusters in the study of fault-zone dynamics, B. Seismol. Soc. Am., 84, 247-263, doi:10.1785/BSSA0840020247.

Nakamura, Y. (1978). A1 moonquakes: source distribution and mechanism, Proc. Lunar and Planet. Sci. Conf. 9th, 3589-360, https://ci.nii.ac.jp/naid/10006236523/en/.

Nooshiri, N., J. Saul, S. Heimann, F. Tilmann et al. (2017). Revision of earthquake hypocentre locations in global bulletin data sets using source-specific station terms, Geophys. J. Int., 208, 589-602, doi:10.1093/gji/ggw405.

Patanè, D., G. Barberi, O. Cocina, P. De Gori et al. (2006). Time-Resolved Seismic Tomography Detects Magma Intrusions at Mount Etna, Science, 313, 821-823, AAAS, doi:10.1126/science.1127724.

Patanè, D., O. Cocina, S. Falsaperla, E. Privitera et al. (2004). Mt. Etna Volcano: A Seismological Framework, in Mt. Etna: Volcano Laboratory, 147-165, AGU, doi:10.1029/143GM10.

Patanè, D., P. De Gori, C. Chiarabba and A. Bonaccorso (2003). Magma Ascent and the Pressurization of Mount Etna's Volcanic System, Science, 299, 2061-2063, AAAS, doi:10.1126/science.1080653.

Patanè, D. and E. Privitera (2001). Seismicity related to 1989 and 1991-93 Mt. Etna (Italy) eruptions: kinematic constraints by fault plane solution analysis, J. Volcanol. Geotherm. Res., 109, 77-98, doi:10.1016/S0377-0273(00)00305-X.

Patanè, D., E. Privitera, F. Ferrucci and S. Gresta (1994). Seismic activity leading to the 1991-1993 eruption of Mt. Etna and its tectonic implications, Acta Vulcanol., 4, 47-55, 10.1016/0377-0273(93)90034-O.

Pavlis, G. L. and N. B. Hokanson (1985). Separated earthquake location, J. Geophys. Res., Solid Earth, 90, 12777-12789, doi:10.1029/JB090iB14p12777.

Podvin, P. and I. Lecomte (1991). Finite difference computation of traveltimes in very contrasted velocity models: a massively parallel approach and its associated tools, Geophys. J. Int., 105, 271-284. doi:10.1111/j.1365-246X.1991.tb03461.x.

Poupinet, G., W. L. Ellsworth and J. Frechet (1984). Monitoring velocity variations in the crust using earthquake doublets: An application to the Calaveras Fault, California, J. Geophys. Res., 89, 5719-5731, doi:10.1029/JB089iB07p05719.

Poupinet, G., F. Glangeaud and P. Cote (1982). P-Time delay measurement of a doublet of microearthquakes, in ICASSP '82, IEEE International Conference on Acoustics, Speech and Signal Processing, 7, 1516-1519, doi:10.1109/ICASSP.1982.1171796.

Richards-Dinger, K. B. and P. M. Shearer (2000). Earthquake locations in southern California obtained using source-specific station terms, J. Geophys. Res., 105, 10939-10960, doi:10.1029/2000JB900014.

Rubin, A. M. and D. Gillard (1998). Dike-induced earthquakes: Theoretical considerations, J. Geophys. Res., Solid Earth, 103, 10017-10030, doi:10.1029/97JB03514.

Ruch, J., S. Pepe, F. Casu, G. Solaro et al. (2013). Seismo-tectonic behavior of the Pernicana Fault System (Mt Etna): A gauge for volcano flank instability?, J. Geophys. Res., Solid Earth, 118, 4398-4409, doi:10.1002/jgrb.50281.

Scarfì, L., M. Aloisi, G. Barberi and H. Langer (2023). Observing Etna volcano dynamics through seismic and deformation patterns, Sci. Rep., 13, 12951, Nature Publishing Group, doi:10.1038/s41598-023-39639-9.

Scotto di Uccio, F., A. Lomax, J. Natale, T. Muzellec et al. (2024). Delineation and Fine-Scale Structure of Fault Zones Activated During the 2014-2024 Unrest at the Campi Flegrei Caldera (Southern Italy) From High-Precision Earthquake Locations, Geophys. Res. Lett., 51, e2023GL107680, doi:10.1029/2023GL107680.

Shearer, P. M., J. L. Hardebeck, L. Astiz and K. B. Richards-Dinger (2003). Analysis of similar event clusters in aftershocks of the 1994 Northridge, California, earthquake, J. Geophys. Res., Solid Earth, 108, doi:10.1029/2001JB000685.

Shelly, D. R., J. L. Hardebeck, W. L. Ellsworth and D. P. Hill (2016). A new strategy for earthquake focal mechanisms using waveform-correlation-derived relative polarities and cluster analysis: Application to the 2014 Long Valley Caldera earthquake swarm, J. Geophys. Res., Solid Earth, 121, 8622-8641, doi:10.1002/2016JB013437.

Sicali, S., G. Barberi, O. Cocina, C. Musumeci et al. (2015). Volcanic unrest leading to the July-August 2001 lateral eruption at Mt. Etna: Seismological constraints, J. Volcanol. Geotherm. Res., 304, 11-23, doi:10.1016/j.jvolgeores.2015.08.004.

Solaro, G., V. Acocella, S. Pepe, J. Ruch et al. (2010). Anatomy of an unstable volcano from InSAR: Multiple processes affecting flank instability at Mt. Etna, 1994-2008, J. Geophys. Res., Solid Earth, 115, doi:10.1029/2009JB000820.

Thorbjarnardottir, B. S. and J. C. Pechmann (1987). Constraints on relative earthquake locations from cross-correlation of waveforms, B. Seismol. Soc. Am., 77, 1626-1634., retrieved from https://pubs.geoscienceworld.org/ssa/bssa/article/77/5/1626/118998.

Tringali, G., D. Bella, F. Livio, M. F. Ferrario et al. (2023). Fault rupture and aseismic creep accompanying the December 26, 2018, Mw 4.9 Fleri earthquake (Mt. Etna, Italy): Factors affecting the surface faulting in a volcano-tectonic environment, Quat. Int., 651, 25-41, doi:10.1016/j.quaint.2021.12.019.

Trugman, D. T. and P. M. Shearer (2017). GrowClust: A Hierarchical Clustering Algorithm for Relative Earthquake Relocation, with Application to the Spanish Springs and Sheldon, Nevada, Earthquake Sequences, Seismol. Res. Lett., 88, 379-391, doi:10.1785/0220160188.

Tucker, W., E. Herrin and H. W. Freedman (1968). Some statistical aspects of the estimation of seismic travel times, B. Seismol. Soc. Am., 58, 1243-1260, GeoScienceWorld, Retrieved from https://pubs.geoscienceworld.org/ssa/bssa/article/58/4/1243/116593/Some-statistical-aspects-of-the-estimation-of.

Waldhauser, F. and W. L. Ellsworth (2000). A Double-Difference Earthquake Location Algorithm: Method and Application to the Northern Hayward Fault, California, B. Seismol. Soc. Am., 90, 1353-1368, GeoScienceWorld, doi:10.1785/0120000006.

Zhou, H. (1994). Rapid three-dimensional hypocentral determination using a master station method, J. Geophys. Res., Solid Earth, 99, 15439-15455, doi:10.1029/94JB00934.

Zollo, A., W. Marzocchi, P. Capuano, A. Lomax et al. (2002). Space and Time Behavior of Seismic Activity at Mt. Vesuvius Volcano, Southern Italy, B. Seismol. Soc. Am., 92, 625-640, GeoScienceWorld, doi:10.1785/0120000287.

***CORRESPONDING AUTHOR: Anthony LOMAX**,
ALomax Scientific, Mouans-Sartoux, France
e-mail: anthony@alomax.net